



Cite this: *Nanoscale Adv.*, 2023, 5, 5799

Oxidation engineering triggered peroxidase-like activity of VO_xC for detection of dopamine and glutathione†

Huimin Jia, Quan Liu,^a Jingjing Si,^a Yuyang Chen,^a Guo Zhou,^a Haihui Lan^b and Weiwei He ^{*a}

MXenes, two-dimensional nanomaterials, are gaining traction in catalysis and biomedicine. Yet, their oxidation instability poses significant functional constraints. Gaining insight into this oxidation dynamic is pivotal for designing MXenes with tailored functionalities. Herein, we crafted VO_xC nanosheets by oxidatively engineering V_4C_3 MXene. Interestingly, while pristine V_4C_3 displays pronounced antioxidant behavior, its derived VO_xC showcases enhanced peroxidase-like activity, suggesting the crossover between antioxidant and pro-oxidant capability. The mixed valence states and balanced composition of V in VO_xC drive the Fenton reaction through multiple pathways to continually generate hydroxyl radicals, which was proposed as the mechanism underlying the peroxidase-like activity. Furthermore, this unique activity rendered VO_xC effective in dopamine and glutathione detection. These findings underscore the potential of modulating MXenes' oxidation state to elicit varied catalytic attributes, providing an avenue for the judicious design of MXenes and derivatives for bespoke applications.

Received 14th August 2023
Accepted 27th September 2023

DOI: 10.1039/d3na00642e
rsc.li/nanoscale-advances

1. Introduction

MXenes, two-dimensional (2D) metal carbides and nitrides, are at the forefront of research due to their potential in energy conversion, catalysis, and biomedicine.^{1–5} Typically, MXenes are derived by selectively etching element A from the MAX phase. The MAX phase conforms to the general formula $\text{M}_{n+1}\text{AX}_n$, where M represents an early transition metal, A belongs to groups 13 or 14 of the periodic table, X is either C or N, and n can be 1, 2, or 3.⁶ Monolayer or few-layered MXenes possess distinctive features: (1) foremost among them is the abundance of hydrophilic functionalities such as $-\text{OH}$, $-\text{O}$, and $-\text{X}$ (where X could be F or Cl). This not only grants MXenes excellent aqueous dispersibility but also facilitates facile chemical modifications, broadening their potential for tailored applications;^{7,8} (2) MXenes host an array of transition metals with mixed valences—typically between 3 and 5. This versatile valence pattern optimizes charge-carrier transfer and

offers a broad spectrum of redox potentials, further enhancing MXenes' functional scope;^{9–12} (3) the majority of MXenes are environmentally benign and display tunable physicochemical properties that hinge upon their elemental makeup. This adaptability accentuates their potential for diverse applications while aligning with sustainability goals.^{13–16} Given the inherently low valence of metals in MXenes, oxidation during preparation and storage becomes inevitable. This spontaneous process can aptly be termed "auto-oxidation".^{17,18} Oxidation significantly alters the physical and chemical properties of MXenes, consequently impacting their functional performance in practical applications. While some studies have addressed the oxidation stability of MXenes and proposed methods to prevent it, the influence of auto-oxidation-induced transformations on MXenes' catalytic behavior remains an area warranting deeper exploration and research.¹⁹

The intrinsic susceptibility of fresh MXenes to oxidation by oxygen imparts them with remarkable antioxidant capabilities. Notably, Ti_3C_2 and V_2C nanosheets have demonstrated a broad-spectrum ability to scavenge reactive oxygen and nitrogen species;^{20–22} the activity of Ti_3C_2 even surpasses that of conventional natural antioxidants by several folds. Given their commendable biocompatibility, MXenes like V_2C , Ti_3C_2 , and Nb_2C , known for their active oxygen species (ROS)-scavenging antioxidant properties, are emerging as promising therapeutics for oxidative stress-induced conditions, such as neuronal damage and acute kidney injury.^{22–25} However, auto-oxidation significantly alters MXenes' redox potentials and valence compositions, potentially steering their chemical and biological activities in

^aKey Laboratory of Micro-Nano Materials for Energy Storage and Conversion of Henan Province, Institute of Surface Micro and Nano Materials, College of Chemical and Materials Engineering, Xuchang University, Xuchang, Henan, 461000, P. R. China.
E-mail: heweiveixu@gmail.com

^bDepartment of Chemistry, Massachusetts Institute of Technology, Cambridge, Massachusetts, 02139, USA

† Electronic supplementary information (ESI) available: Elemental atomic percentages of V_4C_3 and VO_xC calculated by XPS fitted spectra (Table S1); SEM image of MAX phase V_4AlC_3 , multilayered V_4C_3 , few layered V_4C_3 NSs and VO_xC (Fig. S1); diodar optical effect of V_4C_3 nanosheets dilute solution under laser pointer irradiation (Fig. S2); XRD pattern of V_2O_5 after calcination of V_4C_3 nanosheets (Fig. S3). See DOI: <https://doi.org/10.1039/d3na00642e>



different directions at various oxidation phases. For instance, during Ti_3C_2 oxidation, the $Ti^{(II)}$ fraction notably diminishes, while the $Ti^{(IV)}$ content escalates, leading to a marked reduction in its ability to neutralize $\cdot OH$, H_2O_2 , and DPPH radicals.²⁰ MXenes' uncontrollable oxidation in aqueous solutions remains a pivotal constraint for their broader application. In studying the antioxidant behavior of MXenes, we observed a gradient oxidation process, culminating in an irreversible shift from antioxidant to pro-oxidant activities. This transition can instigate unforeseen biological consequences.

In our investigation, we primarily aim to decipher the impacts of oxidation on the structural and catalytic attributes of MXenes, with V_4C_3 MXene spotlighted as our model. This choice is motivated by vanadium's rich valence states (+2, +3, +4, and +5) and the inherent stability of the atomic configuration. Freshly prepared V_4C_3 MXene nanosheets demonstrate an impressive capability to scavenge free radicals, underscoring their antioxidant prowess. Through controlled oxidation of a few-layered V_4C_3 , we synthesized VO_xC nanosheets that adopt an intricately entangled morphology. The rise of nanozymes—nanostructures mimicking enzymatic properties—has garnered significant interest due to their exceptional merits and broad application spectrum.^{26–28} Intriguingly, the VO_xC nanosheets we prepared manifest robust peroxidase (POD)-like activity. This is attributable to the mixed valence states within the VO_xC , which bolster the Fenton reaction cycle involving V^{n+} species and H_2O_2 , perpetuating the generation of hydroxyl radicals. Leveraging the antagonistic influence of biomolecules on this POD-like behavior, we devised a proficient and sensitive colorimetric assay for the detection of dopamine and glutathione.

2. Experimental section

2.1 Chemical and materials

V_4AlC_3 MAX powder (400 mesh) was purchased from 11 Technology, hydrogen peroxide (H_2O_2), horseradish peroxidase (HRP), dopamine hydrochloride, dimethyl sulfoxide (DMSO), hydrofluoric acid (HF) and 3,3',5,5'-tetramethylbenzidine (TMB) were purchased from Sinopharm Chemical Reagent Co., Ltd. (Beijing, China) and 2,2'-Azinobis-(3-ethylbenzthiazoline-6-sulphonate) (ABTS) were commercially available from Aladdin Industrial Co (CA, USA). L-Glutathione (GSH) were purchased from Beijing OKA Biotechnology Co., LTD. Potassium persulfate ($K_2S_2O_8$) were purchased from Shanghai Maclin Biochemical Technology Co., LTD. Pure terephthalic acid (PTA) were purchased from Thermo Fisher Scientific. Tetramethyl ammonium hydroxide (TMAOH) were purchased from Sigma-Aldrich (Shanghai, China). Milli-Q water ($18\text{ M}\Omega\text{ cm}$) was used in the preparation of all solutions. All glassware and autoclave used in the following procedures were cleaned by aqua regia solution ($HNO_3/HCl = 1:3$ v/v).

2.2 Characterization

UV-vis absorption spectra were obtained using a Cary 60 UV-Vis Spectrometer (Varian, USA) and a matched quartz cuvette with a path length of 1 cm. The crystal structures of the V_4C_3 and VO_xC

nanosheets were characterized by X-ray diffraction (XRD, D8 Advance diffractometer, Bruker, Germany) using monochromatized $Cu K\alpha$ radiation ($\lambda = 1.5418\text{ \AA}$). Transmission electron microscope (TEM) and high-resolution transmission electron microscope (HRTEM) were captured on a Tecnai G2 F20 U-Twin electron microscope with an accelerating voltage of 200 kV. SEM images were obtained by FEI Field Emission Scanning Electron Microscope (FE-SEM), USA. Fourier transform infrared spectroscopy (FT-IR) were acquired by Thermo Fisher Nicolet 6700 infrared spectrometer. X-ray photoelectron spectroscopy (XPS) was performed with a Thermo ESCALAB 250XI multifunctional imaging electron spectrometer (Thermo Fisher Scientific, USA) using 150 W $Al K\alpha$ radiation and a base pressure of approximately 3×10^{-9} mbar. The binding energies were calibrated to the C 1s line at 284.8 eV. Fluorescence spectral signals were acquired by a Hitachi F-4600 fluorescence spectrometer, Japan. The measurements were carried out at room temperature under the following conditions: microwave power 2 mW, modulation amplitude 1.0 G, attenuation 20 dB, and scan range of 100 G.

2.3 Synthesis of VO_xC nanosheets

Preparation of multilayer V_4C_3 nanosheets. 1 g of V_4AlC_3 was added to a 100 mL Teflon tank and then 20 mL of hydrofluoric acid (HF, 40%) was carefully added in a fume hood. After sealing the reactor, it was stirred and reacted at room temperature for 14 days to obtain a multilayer V_4C_3 solution in which the Al layer was etched away. The product was washed by centrifugation several times with deionized water (3500 rpm) to $pH > 6$. The product was dried under vacuum at 60 °C for 12 h to obtain dried V_4C_3 powder.

Preparation of few layers V_4C_3 MXene. Firstly, 0.1 g multilayer V_4C_3 powder was weighed into a 10 mL glass sample bottle, and 5 mL high concentration tetramethylammonium hydroxide solution (TMAOH, 25% aqueous solution) was added, and stirred at room temperature (25 °C) for 3 days. The TMAOH solution was then centrifuged three times at 8000 rpm. The black precipitates were re-dispersed into 20 mL deionized water, and the 2D V_4C_3 solution was obtained by ultrasound under argon atmosphere for 90 min. The precipitation was then removed by centrifugation at 8000 rpm for 20 min and a 2D V_4C_3 nanosheets colloidal solution was collected. The 2D V_4C_3 nanosheets is dried in a vacuum freeze dryer for at least 24 h and then collected for quantification.

Preparation of VO_xC nanosheets. V_4C_3 nanosheets is prepared into a solution of 1 mg mL^{-1} and placed in a stripped sample bottle with the solution filling not exceeding 50%. The sample bottle was placed at 40 °C for 72 h until the solution was a light dark green state.

Preparation of V_2O_5 . The V_4C_3 nanosheets was freeze-dried to obtain a black light powder, which was placed in a porcelain pot and calcined in a Muffle furnace at a heating rate of 5 °C min^{-1} and held for 3 h. After cooling, the powder was yellow.

2.4 Evaluation of total antioxidant activity

The antioxidant capacity of nanosheets was assessed by ABTS assay. Firstly, the stable free radical ABTS^{•+} was freshly



made by dissolving 0.0374 g ABTS and 0.0066 g $K_2S_2O_8$ in 30 mL deionized water for 12 h in dark, and the solution was diluted by 20 times before use. The antioxidant capacity of V_4C_3 nanosheets at different oxidation stages was tested by UV-vis absorption spectroscopy. In typical, 10 μ L V_4C_3 or VO_xC nanosheets (0.5 mg mL^{-1}) was added to 3 mL ABTS⁺ solution, and the absorption spectrum was recorded with two minutes interval. The scavenging rate was calculated by plotting the absorbance at 730 nm in function of reaction time.

2.5 POD-like enzyme activity and enzymatic kinetics test

The POD-like activity of VO_xC nanosheets has been tested by using TMB assay. In typical, 20 μ L 20 mM TMB and 20 μ L 0.1 M H_2O_2 were mixed in 3 mL H_2O or 10 mM HAc-NaAc buffer with different pH. Then, 10 μ L of V_4C_3 or VO_xC (0.2 mg mL^{-1}) was added to accelerate the oxidation of TMB. The UV-vis absorption spectra evolution was recorded using the scanning kinetics model with 1 min interval. The absorbance at 650 nm *vs.* reaction time was plotted to calculate the catalytic reaction kinetic parameters.

The apparent steady-state kinetic measurements were carried out. For TMB and H_2O_2 as substrate, the enzymatic kinetic parameters, *Michaelis* constant (K_m) and maximal reaction velocity (V_{max}), were calculated according to the *Michaelis-Menten* equation:

$$1/v = K_m/V_{max} \times (1/[S]) + 1/V_{max}$$

where v is the reaction initial velocity and $[S]$ is the concentration of the substrate.

2.6 Detection of dopamine and glutathione

Detection of dopamine. The colorimetric detection of dopamine based on the concentration-dependent inhibition of VO_xC POD-like activity was performed. Typically, dopamine is configured in a solution of 2 mM concentration. To ensure the accuracy of the experiment, the total solution of the sample to be tested was strictly controlled to be 3 mL. Therefore, during the test, x μ L of dopamine solution was added to $2940-x$ μ L ($x = 10, 20, 30, 40, 50, 60$) deionized water. Next, 20 μ L of 20 mM TMB solution and 20 μ L of 0.1 M H_2O_2 solution were added, followed by 20 μ L of 0.2 mg mL^{-1} VO_xC solution, immediately mixed for timing, and UV-vis absorption spectrum data began to be recorded when the reaction lasted for two minutes, with a monitoring range of 800–400 nm. With this method, at least three repeated tests were performed to measure different amounts of dopamine.

Detection of glutathione. Similarly, colorimetric detection of glutathione was performed based on the concentration-dependent inhibition of POD-like activity by glutathione. Normally, glutathione is configured in a solution of 0.5 mM concentration. To ensure the accuracy of the experiment, the total solution of the sample to be tested was strictly controlled to be 3 mL. Therefore, during the test, x μ L glutathione solution was added to $2940-x$ μ L ($x = 10, 20, 30, 40, 50, 60, 70, 80, 140$) deionized water. Next, 20 μ L of 20 mM TMB solution and 20 μ L

of 0.1 M H_2O_2 solution were added, followed by 20 μ L of 0.2 mg mL^{-1} VO_xC solution, immediately mixed for timing, and ultraviolet-visible absorption spectrum data began to be recorded when the reaction lasted for two minutes, with a monitoring range of 800–400 nm. The method was used to perform at least three repeatable tests for different levels of glutathione.

3. Results and discussion

3.1 Formation of VO_xC via oxidation engineering of V_4C_3

As delineated in Fig. 1, we introduce a meticulously designed protocol to fabricate VO_xC nanosheets. The genesis of these nanosheets stems from a systematic oxidation engineering of few-layered (FL) V_4C_3 MXene nanosheets under controlled conditions at 40 °C. For this endeavor, V_4AlC_3 MAX phase, characterized by its dense 3D layered architecture, was judiciously selected as the foundational precursor. To realize the FL- V_4C_3 nanosheets, we employed the well-established HF etching technique, followed by a 25% TMAOH intercalation process (Fig. S1a–c†).²⁹ As inferred from the TEM imaging (Fig. 2a), the newly synthesized V_4C_3 nanosheets display dimensions ranging from 300 to 500 nm. These nascent nanosheets bear a multitude of hydrophilic moieties (–OH, –F, –O) on their surface, thereby facilitating an excellent dispersion in aqueous solutions and manifesting the quintessential Tyndall phenomena, as depicted in Fig. S2.† Recognizing the inherent propensity of the FL- V_4C_3 nanosheets, especially in their fresh state, towards oxidation in aqueous environments—predominantly due to the extensive presence of low-valence vanadium—we embarked on a systematic study of their oxidation dynamics.¹² Consequently, we deliberately undertook the oxidation process of V_4C_3 under a carefully controlled condition at 40 °C. Upon exposure to a heat treatment at 40 °C for a span of 72 h, the V_4C_3 MXene nanosheets undergo a transformation to form their oxidation derivatives, VO_xC nanosheets, as vividly depicted in Fig. 2b and S1d.† Intriguingly, these VO_xC nanosheets exhibit a characteristic belt-like morphology, reminiscent of thin, delicately curled sheets, and boast an impressive span, extending beyond the 2 μ m mark.

The HRTEM revealed the intricate lattice fringe of VO_xC . An adjacent planar separation was meticulously calculated to be 0.205 nm, corresponding to the (002) plane of VO_xC , as showcased in Fig. 2c. XRD served as an instrumental technique in deciphering the crystalline structures of both V_4C_3 and VO_xC . A noteworthy observation is the vanishing of the (004), (006), and (008) diffraction peaks of V_4C_3 . Concurrently, the (002) diffraction peaks of V_4C_3 migrate to an elevated angle with a pronounced diminution in intensity as oxidation time escalates, as highlighted in Fig. 2d and e. Most strikingly, the diffraction peak of V_4C_3 nanosheets exhibits a steady decline and vanishes post 20 h, underscoring the hypothesis that oxidation precipitates the degradation and ensuing amorphization of V_4C_3 nanosheets. As oxidation ensues, the (002) diffraction peak makes a re-emergence post the 60 h mark, signifying the orchestrated re-organization and recrystallization of VO_xC . This underpins a transformative pathway for VO_xC , reminiscent of a “breakage-followed-by-



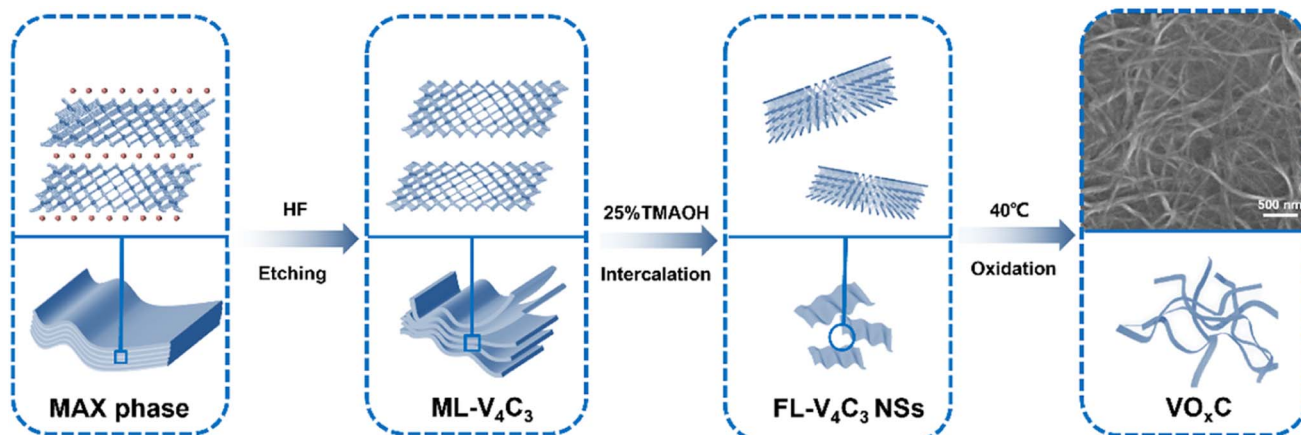


Fig. 1 Schematic illustration for the synthesis and structure diagram of VO_xC nanosheets.

reconstruction" paradigm, while ensuring the resultant VO_xC retains its quintessential layered MXene crystalline structure.

The dynamism of the UV-vis spectra of the V_4C_3 suspension, mapped across the span of oxidation at 40 °C, delineates the shifting optical properties inherent to the metamorphosis from V_4C_3 to VO_xC . Of particular note are the emergent peaks at wavelengths 280 and 400 nm, serving as hallmarks of the VO^{2+} absorption band. This further corroborates the reconstruction narrative of VO_xC , mirroring findings from the XRD analysis (Fig. 2f).

Furthermore, the oxidative journey begets a palpable expansion in the DLS diameter, evolving from ~ 250 nm in V_4C_3 to ~ 350 nm in VO_xC (Fig. 2g). Concurrently, we witness a declination in zeta potential values, transitioning from -44.8 mV to a more subdued -29.6 mV (Fig. 2h). FT-IR was instrumental in corroborating shifts in the surface functional group composition and bond structuring pre- and post-oxidation (Fig. 2i). The spectra for VO_xC are indicative of a discernible attenuation in the $-\text{OH}$ signal juxtaposed against an escalation in the $\text{C}=\text{O}$ signal intensity, a trend that resonates with the increased tethering of oxygen during oxidation.

Cumulatively, these revelations shed light on profound transformations in morphology, dimensions, crystallinity, surface characteristics, and optical nuances associated with V_4C_3 and its oxidized counterpart, VO_xC . This underscores the pivotal role auto-oxidation plays in sculpting the MXene framework. Providentially, this lends an intuitive avenue to fathom the structure–activity nexus, thereby facilitating the nuanced tailoring of MXene functionalities.

Beyond the notable metamorphosis in atomic structure, V_4C_3 's oxidation journey substantially reconfigures both its elemental composition and bond disposition. The XPS survey spectra vouch for the concurrent presence of V, C, and O across both the V_4C_3 and VO_xC spectra, as illuminated in Fig. 3a. Intriguingly, while elemental consistency persists, a remarkable oxygen upsurge is discerned. Spectrum analysis reveals an escalation in the oxygen fraction, notably surging from 25.23% in V_4C_3 to 43.10% in VO_xC . A deeper dive into the bonds

suggests that this newly incorporated oxygen predominantly pairs with V in a V–O arrangement, as detailed in Table S1.†

In the meticulous V 2p high-resolution XPS spectra of V_4C_3 nanosheets, four distinct deconvolutional peaks emerge. These correspond to the diverse states: V–C (V^{2+}), V^{3+} , V^{4+} , and V^{5+} . The manifestation of V^{4+} and V^{5+} signals might owe their presence to incidental oxidation of V_4C_3 during storage and subsequent measurements. On the other hand, the discerned doublet peaks in VO_xC echo the signatures of V^{3+} , V^{4+} , and V^{5+} .^{30,31} Astoundingly, post-oxidative treatment, the V–C bond in VO_xC ceases to exist, highlighting the formation of VO_xC as a nuanced tapestry of mixed valence vanadium oxide, as exemplified in Fig. 3b. Diving deeper into the valence intricacies, a coexistence of multiple vanadium valences is evident in both V_4C_3 and VO_xC . V_4C_3 is predominantly colored by lower valences, with V^{2+} and V^{3+} jointly accounting for approximately 60% and cumulatively reaching near 90% with V^{4+} . In stark contrast, VO_xC showcases V^{4+} as the dominant player at about 50%, flanked by roughly equal contributions from V^{3+} and V^{5+} .

Pivoting to the C 1s spectrum of V_4C_3 nanosheets, the analysis discerns four Gaussian peaks, symbolizing V–C, C–C, C–H, and C–O. Herein, the V–C peak is conspicuously absent post-oxidation, accompanied by a diminution in the C–H peaks, while the C–C and C–O peaks see a significant surge in intensity, as captured in Fig. 3c. The orchestrated O 1s peaks, signifying varied oxygen bonds in $\text{V}–\text{C}(\text{OH})_x$, $\text{C}=\text{O}$, $\text{V}–\text{O}$, and $\text{V}–\text{O}_x$, buttress the assertion of a marked augmentation in bound V oxygen, a narrative articulated in Fig. 3d.

Collectively, through mentioned above analytical techniques (TEM, XRD, XPS, etc.), the oxidation proceeding mechanism have been uncovered. With the oxidation proceeding, the morphology, size distribution, crystal structure, chemical element, and valence compositions have changed dramatically, underscoring the V_4C_3 nanosheets go through destruction, disintegration, and reconstruction to form VO_xC nanosheets. These insights paint a compelling picture of the oxidation's transformative potential, underscoring its finesse in masterfully orchestrating the chemical and valence tapestry of MXenes.



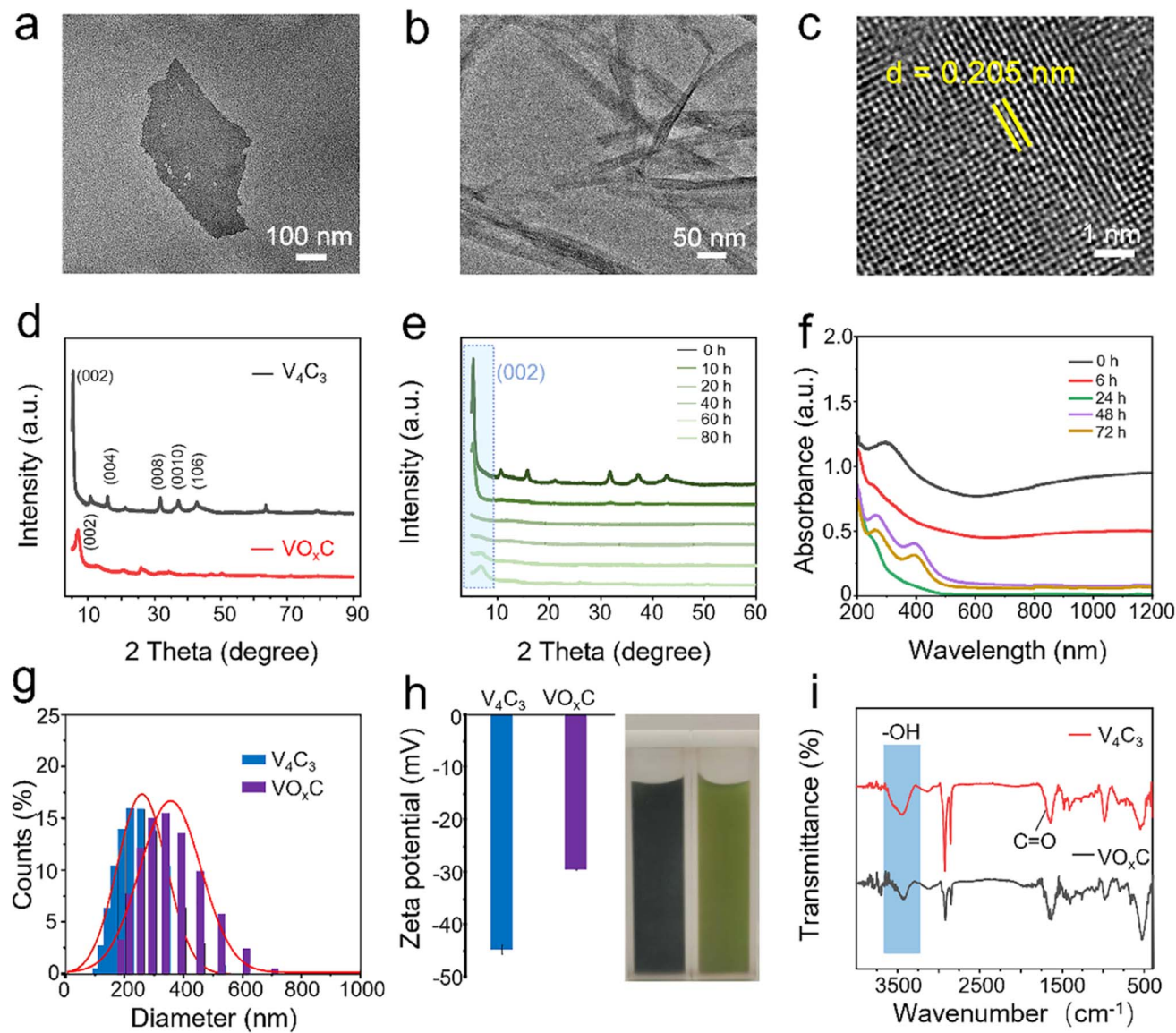


Fig. 2 Characterization of V_4C_3 and VO_xC nanosheets. (a) TEM image of fresh V_4C_3 nanosheets; (b) TEM and (c) HRTEM images of VO_xC nanosheets after auto-oxidation treatment for 72 h at 40 °C; (d) XRD patterns of fresh V_4C_3 and VO_xC nanosheets; (e) XRD patterns of V_4C_3 at different oxidation times; (f) UV-vis absorption spectra of V_4C_3 at different oxidation times; (g) kinetic dimension comparison of fresh V_4C_3 and VO_xC nanosheets; (h) zeta potential comparison and optical image of fresh V_4C_3 and VO_xC nanosheets; (i) FT-IR comparison before and after oxidation of fresh V_4C_3 and VO_xC nanosheets.

3.2 Oxidation engineering triggered the POD-like activity of VO_xC nanosheets

The auto-oxidative process introduces profound shifts in the redox potential of V_4C_3 nanosheets, catalyzing unanticipated biological activities. Predominantly, the antioxidant prowess emerges as a central narrative. The evolution of the antioxidant disposition of V_4C_3 nanosheets through the oxidation arc holds paramount significance in biological contexts. Our meticulous exploration unveiled that nascent V_4C_3 nanosheets exhibit a flair for ROS scavenging, underscoring their remarkable antioxidant fortitude. To distill the core of this study, we gauged antioxidant efficacy through the lens of the total antioxidant capacity (TAC), facilitated by the reduction of ABTS^+ . This

entity, borne from the oxidation of ABTS via $\text{K}_2\text{S}_2\text{O}_8$, is a staple in TAC assays. Parallelly, the pro-oxidant mettle was mapped via its prowess in orchestrating TMB oxidation, a chromogenic substrate emblematic of POD-like activity assays. This oxidation typically manifests as a distinctive blue hue, characterized by its unique absorption spectrum. In their pristine state, V_4C_3 nanosheets can deftly quench ABTS^+ , resonating with their antioxidant acumen, yet remain inert to catalyzing TMB oxidation in an H_2O_2 milieu.

However, as oxidation progresses, a captivating narrative unfolds: the once dominant antioxidant efficacy, as gauged by ABTS^+ reduction, wanes progressively until it vanishes (Fig. 4a). Intriguingly, after an incubation of 40 h, the once dormant

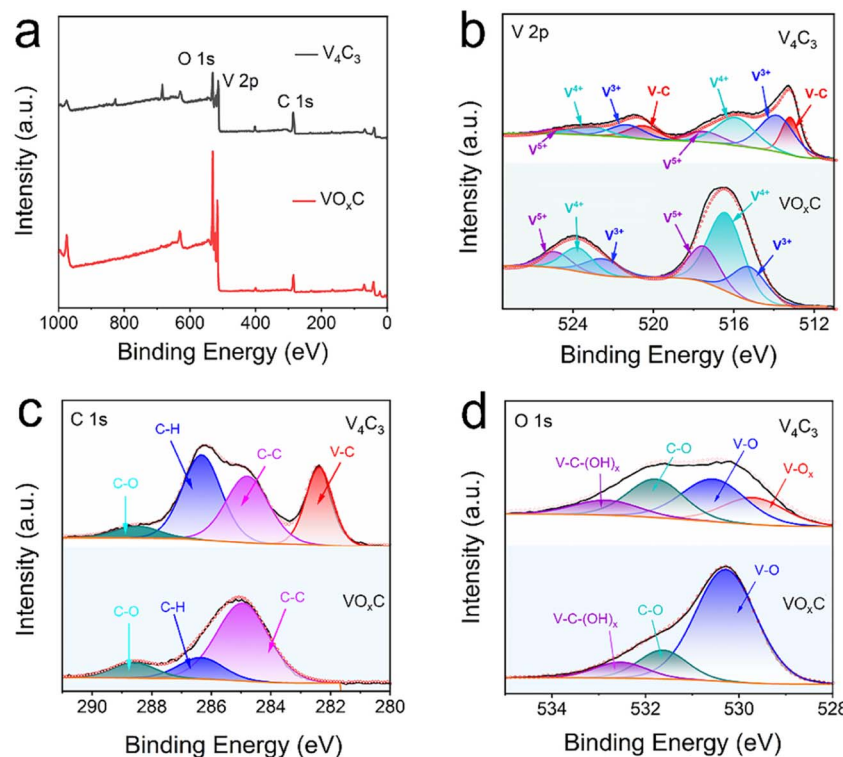


Fig. 3 XPS spectra of VO_xC nanosheets. (a) Survey spectra; (b–d) high-resolution fitted spectra of V 2p, O 1s, and C 1s.

POD-like dynamism to drive TMB oxidation stirs to life, amplifying subsequently (Fig. 4a). These crescendo peaks post a 60 h oxidation interval, where the POD zeal reaches its zenith and the ABTS⁺ quenching capability plunges to its nadir. Fig. 4b and c vouch for the capability of VO_xC in spearheading TMB oxidation in an H_2O_2 backdrop and a time-centric paradigm, devoid of any oxidase (OXD)-like undertones. Fig. 4a encapsulates this transformational journey, portraying the poignant intersection between antioxidant and pro-oxidant trajectories around the 40 h mark during the V_4C_3 nanosheet oxidation. This empirical revelation underscores the crux of our findings: V_4C_3 oxidation is the linchpin that pivots the sheets from their inherent antioxidant stature to a newfound pro-oxidant persona, replete with intrinsic POD-like activity.

Temperature is pivotal in governing the oxidation kinetics of V_4C_3 and subsequently sculpting the emergence of VO_xC . Indeed, it's conceivable that such variations could inflect the nuances of POD activity. To unravel this thermodynamic interplay, we embarked on a systematic investigation spanning four distinct oxidation temperatures: 40 °C, 50 °C, 60 °C, and 70 °C. Our objective was to chart the interplay between POD-like activity and the temperature trajectory.

As illustrated in Fig. 4d, VO_xC , when nurtured at 40 °C, reaches the zenith of POD-like activity. However, a captivating trend emerges with escalating temperatures. Each incremental rise attenuates the POD prowess of the resulting VO_xC nanosheets. To present a stark contrast, V_4C_3 nanosheets underwent rigorous oxidation through calcination at 500 °C in an air milieu, culminating in the formation of V_2O_5 nanocrystals

(Fig. S3†). When juxtaposed, the POD-like dynamism of VO_xC (birthed at 40 °C) conspicuously outshines, being an astounding 5.5-fold more potent than its V_2O_5 counterpart (Fig. 4e).

Further exploration into the catalytic nuances of VO_xC led to a systematic assessment of its responses to variations in pH, as well as H_2O_2 and TMB concentrations, as depicted in Fig. 4f–h. Intriguingly, VO_xC 's optimal catalytic activity manifested at a pH of 5.0. This pH mark stands marginally elevated compared to canonical nano-peroxidases, suggesting a unique response profile for VO_xC in the nano-peroxidase family.³² The concentration of H_2O_2 shares the same trends on affecting the catalytic rate, which is positively proportional to H_2O_2 and TMB concentration in the detection range. By fitting the typical double reciprocal plots ($1/v$ vs. $1/[S]$) to the *Michaelis-Menten* equation, we calculated the enzyme kinetic parameters of VO_xC as peroxidase using H_2O_2 and TMB as substrate, respectively (Fig. 4e and g). When TMB is the substrate, the *Michaelis* constant (K_m) and maximum reaction velocity (V_{\max}) was calculated to be 0.01912 mM and 9.745×10^{-6} M s⁻¹, respectively. When H_2O_2 is substrate, the K_m and V_{\max} of VO_xC were calculated to be 1.54 mM and 33.45×10^{-6} M s⁻¹, respectively. This test results suggest that VO_xC exhibited superior POD-like activity. To reveal the POD-like catalytic mechanism, the production of hydroxyl radicals in the presence of VO_xC and hydrogen peroxide was determined by fluorescence spectroscopy. TA is selected as the fluorescent probe to $\cdot\text{OH}$. The results showed a stronger fluorescence signal after the mixture of TA,



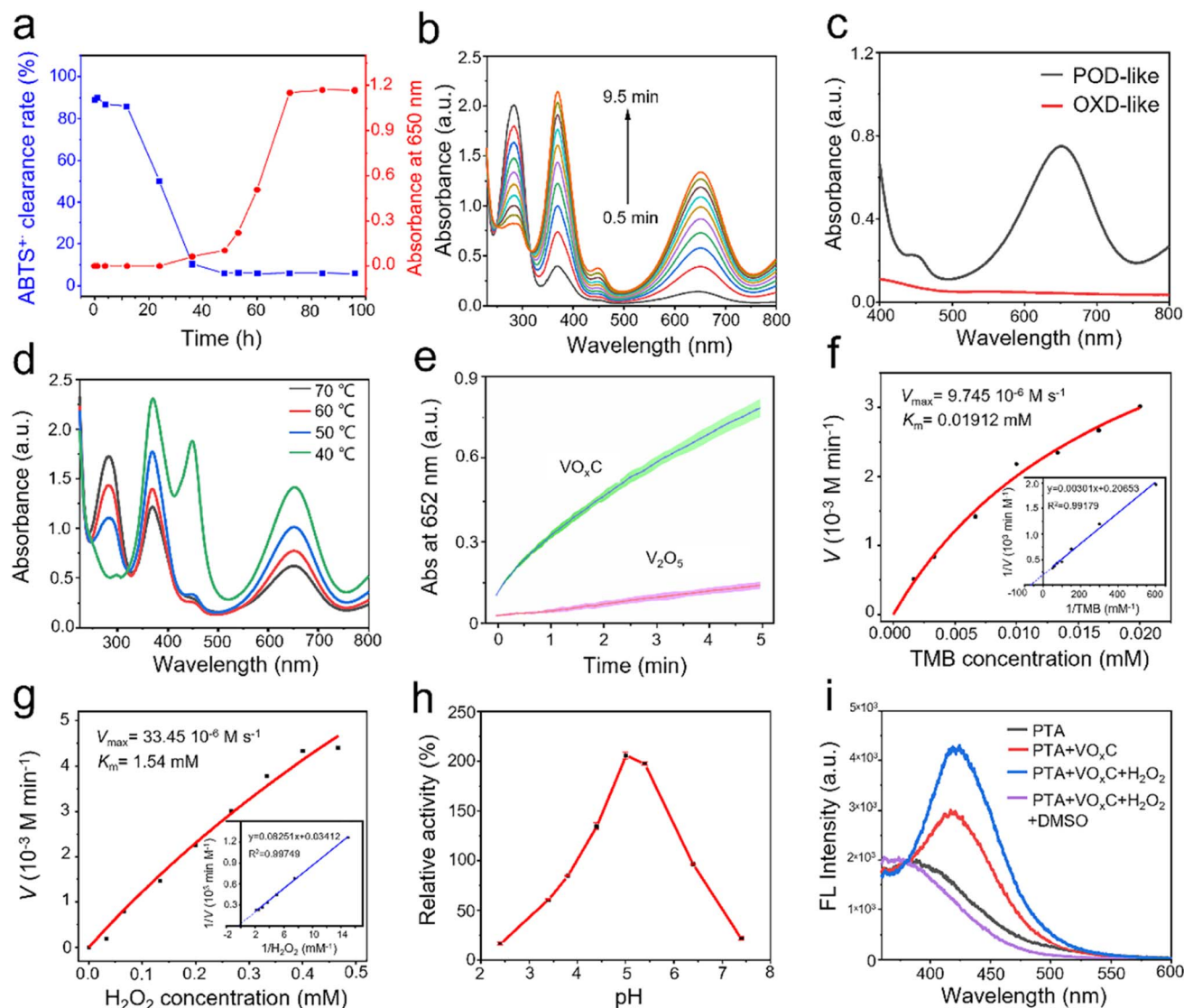


Fig. 4 POD-like activity of VO_xC . (a) The transformation of antioxidant and POD-like activity during the oxidation process; (b) kinetic absorption spectra of H_2O_2 oxidation of TMB catalyzed by VO_xC ; (c) comparison of TMB absorption spectra of VO_xC catalytic oxidation with and without H_2O_2 ; (d) the comparison of VO_xC prooxidation activities at different oxidation temperatures; (e) comparison the POD-like activity of VO_xC and V_2O_5 ; (f–g) effect of TMB and H_2O_2 concentration on the rate of VO_xC catalytic oxidation of TMB; the illustration shows the corresponding double reciprocal plots; (h) relative POD activity at different pH values; (i) fluorescence spectra of hydroxyl captured by PTA.

VO_xC and H_2O_2 , and the signal could be removed by typical $\cdot\text{OH}$ scavenger DMSO, demonstrating the generation of $\cdot\text{OH}$.

3.3 Possible mechanism for POD-like activity

Drawing from our comprehensive analysis, a conceptual trajectory detailing the metamorphosis from V_4C_3 to VO_xC emerges (Fig. 5a). Initiated by oxidative interactions, the resilient V–C bonds are compromised, leading to a substantial alteration in the initial structural framework. As the oxidation journey continues, there's a subsequent structural renaissance marked by the reorganization and re-crystallization of the VO_xC nanocrystals. This transformative sequence culminates in pronounced shifts in both morphology and chemical composition (Fig. 5b).

Pivoting to the underlying mechanics of POD-like activity, we venture into the domain of valence engineering. The canonical Fenton or Fenton-like processes, underpinned by the interaction between H_2O_2 and specific transition metal ions (notably Fe^{2+} and Cu^{2+}), have been acclaimed for their prowess in spawning hydroxyl radicals through reaction (1). Many studies are reporting the POD-like activity of nanomaterials is attributed to hydroxyl radicals' production based on Fenton reactions.³³



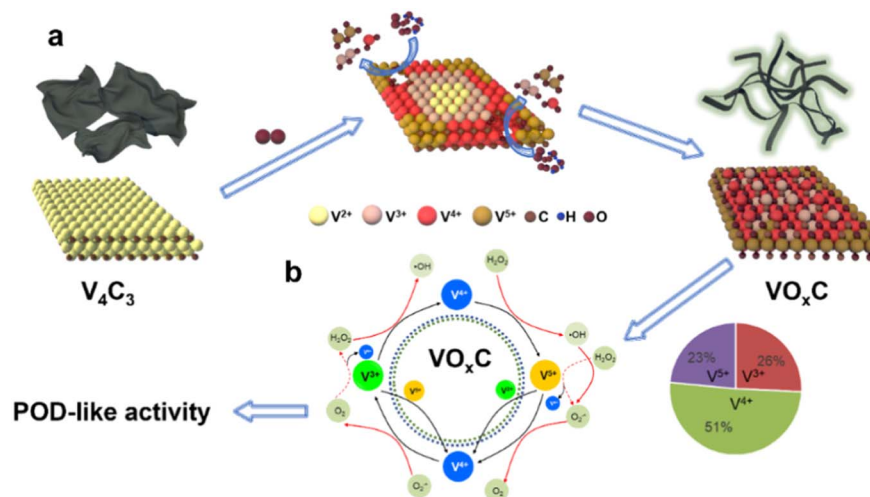
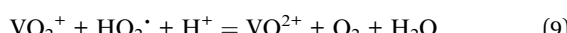
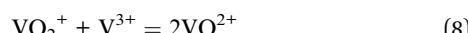
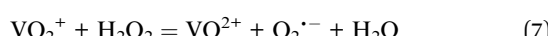
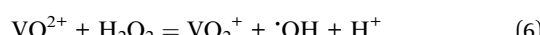
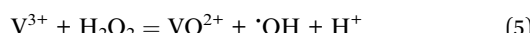


Fig. 5 The schematic diagram for the (a) formation mechanism of VO_xC and (b) the valence engineering driven catalytic mechanism for POD-like activity of VO_xC .



Vanadium complexes represent an important kind of catalysts in chemical and biological applications because of their unique electronic property.³⁴ In our VO_xC , the chemistry of vanadium is accessible with 3 adjacently mixed valence states +3 to +5 in an aqueous solution. As we calculated above, oxidation can balance the V valence compositions. The proportional composition of V^{3+} , V^{4+} and V^{5+} in VO_xC is 26%, 51% and 23%, respectively. Such mixed valence state with V^{4+} dominating possesses abundant electron transport behaviors. The standard redox half-reactions for $\text{H}_2\text{O}_2/\text{H}_2\text{O}$, $\text{VO}_2^+/\text{VO}^{2+}$ and $\text{VO}^{2+}/\text{V}^{3+}$ are shown above.³⁵ Theoretically, either V^{3+} and V^{4+} can react with hydrogen peroxide to generate hydroxyl radicals based on Fenton mechanisms (eqn (5) and (6)).³⁶



Strikingly, the VO_2^+ species can be reduced back to VO^{2+} through three pathways, as depicted in eqn (7)–(9). These routes allow for the completion of the cycle. Owing to the presence of mixed valences, it is hypothesized that there are multiple pathways to produce hydroxyl radicals, as well as four pathways for the regeneration of VO^{2+} and V^{3+} . This maintains the cycle (Fig. 5b). As a result, VO_xC exhibits a highly efficient and persistent ability to generate hydroxyl radicals, demonstrating robust and sustained POD-like activity.

Notably, it is important to understand why the freshly prepared V_4C_3 does not exhibit POD-like activity or generate hydroxyl radicals. The freshly prepared V_4C_3 , which has

undergone minimal oxidation, mainly comprises vanadium in lower valence states. The V^{2+} , V^{3+} and V^{4+} not only have the potential to produce hydroxyl radicals based on the Fenton mechanism, but they also act as potent reducing agents capable of reducing $\cdot\text{OH}$ and H_2O . This results in complex reaction dynamics.

The rich presence of low-valence states with strong electron-donating capabilities can effectively and quickly reduce highly active $\cdot\text{OH}$, explaining the observed phenomena. These findings highlight that the valence composition of mixed-valence vanadium is critical in regulating biological activities, such as antioxidant and pro-oxidant behaviors. In this study, we demonstrated that controlling auto-oxidation provides a potential strategy for regulating valence composition.

3.4 Detection of dopamine and glutathione

The inherent POD-like functionality of VO_xC has remarkable implications not just in the realm of catalysis, but also in the domain of biological detection. Dopamine, a pivotal neurotransmitter and hormone, assumes significant interest due to its potential dysregulation, leading to a multitude of health disorders. An overexpression can trigger conditions like mania, obesity, and addictive behaviors, whereas a deficiency is often linked to Parkinson's disease and attention deficit hyperactivity disorder. Thus, the importance of accurate detection of dopamine for managing health conditions can't be overstated.

In our investigations, we discovered that the POD-like activity of VO_xC could be suppressed by dopamine, consequently slowing down the oxidation of TMB. Interestingly, this inhibition was found to be dependent on the concentration of dopamine, which sets the foundation for the colorimetric detection of this neurotransmitter. We designed experiments in which the concentrations of VO_xC , H_2O_2 , and TMB were kept constant while varying the dopamine concentrations. As dopamine was introduced, we observed a decrease in absorbance at 650 nm, indicating a reduction in TMB oxidation (Fig. 6b).

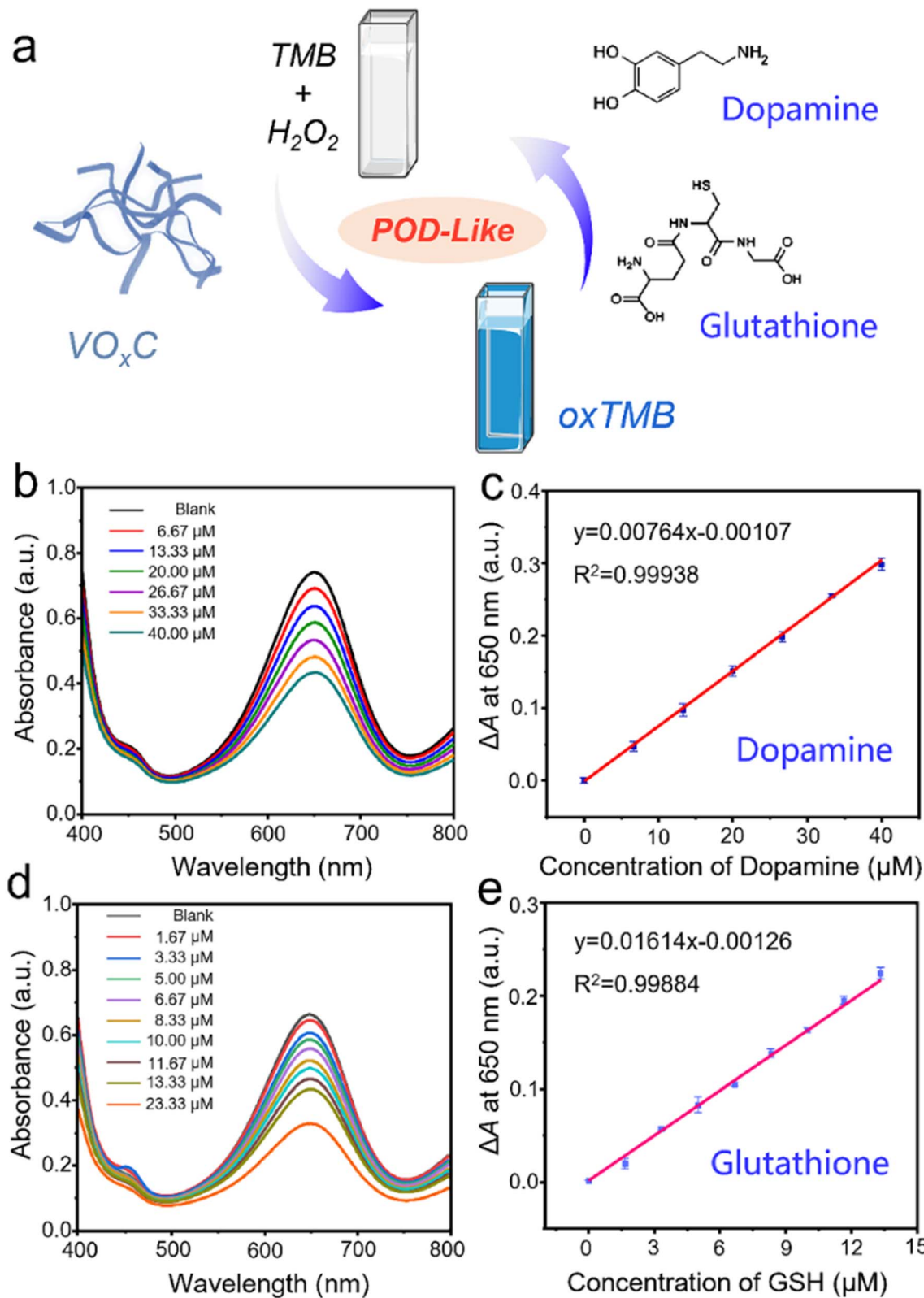


Fig. 6 Detection of dopamine and glutathione by using the POD-like activity of $VO_x C$. (a) Scheme of the inhibitory mechanism for biomolecular detection. (b) The UV-vis absorption spectrum evolution in the absence and presence of dopamine with different concentrations. (c) The dependence of ΔA at 650 nm on the concentration of dopamine. (d) The UV-vis absorption spectrum evolution in the absence and presence of glutathione with different concentrations. (e) The dependence of ΔA at 650 nm on the concentration of glutathione.

Following this, we plotted a response curve of $A_0 - A$ (ΔA), where A_0 denotes the absorbance of the control group and A represents the absorbance in the presence of varied dopamine concentrations. The plot displayed a robust linear relationship ($R^2 = 0.999$) within the dopamine concentration range of 6.67–40 μM , with the limit of detection (LOD) for dopamine determined to be 2.5 μM ($S/N = 3$) (Fig. 6c). Interestingly, dopamine molecules, with their amino and phenolic hydroxyl groups, have the potential to act as electron donors, reducing H_2O_2 and leading to the formation of dopamine-*o*-quinone. This involvement of dopamine competes with TMB for H_2O_2 consumption, thereby reducing the amount of H_2O_2 involved in TMB oxidation and subsequently leading to a decrease in absorbance at 650 nm. This intriguing discovery underscores the potential utility of VO_xC in dopamine detection.

Often hailed as “The Mother of All Antioxidants,” glutathione occupies a pivotal position in biological systems, instrumental in governing immune responses and determining longevity. A scarcity of this antioxidant in the body frequently correlates with numerous chronic ailments and diseases. In a manner mirroring dopamine, glutathione’s potent antioxidant properties can also stifle the POD-like activity of VO_xC . Seizing upon this inhibitory paradigm, we engineered a colorimetric assay for glutathione detection. Maintaining consistent concentrations of VO_xC , H_2O_2 , and TMB, we varied glutathione levels within controlled bounds. Our observations conclusively revealed that the oxidation rate of TMB is markedly suppressed by glutathione, and this suppression is strikingly concentration-dependent (Fig. 6d).

Further analysis provided a lucid view: plotting the response ΔA at 650 nm against glutathione concentrations spanning from 1.67 to 23.33 μM unveiled a tight linear correlation, as evident from an R^2 value of 0.9988. This assay demonstrated an impressive LOD for glutathione, pegging it at 0.36 μM . Therefore, leveraging the unique POD-like properties of VO_xC nanosheets presents an elegant and efficient route to detect crucial bio-analytes like dopamine and glutathione, further enriching the palette of analytical tools in biomedicine.

4. Conclusion

In conclusion, the POD-like activity of VO_xC nanosheets triggered by oxidatively engineering V_4C_3 MXene was presented in this work. With the oxidation proceeding, the V_4C_3 nanosheets go through destruction, disintegration, and reconstruction to form VO_xC nanosheets and the morphology, size distribution, crystal structure, chemical element, and valence compositions have changed dramatically. Especially, V_4C_3 is a non-enzymatic antioxidant that can scavenge free radicals, while the VO_xC shows superior POD-like activity to generate hydroxyl radicals. The valence engineering-driven mechanism underlying the POD-like activity was proposed, the oxidation balanced the valence composition of V in VO_xC that can facilitate the Fenton reaction through multiple pathways to persistently produce hydroxyl radicals. Based on the inhibitory effect on the POD-like activity of VO_xC , a facile method has been developed for the detection of dopamine and glutathione. Although oxidation

instability has been considered as the bottleneck challenge in MXenes development, it, fortunately, provides a facile way to delicately treat MXenes and produce various derivates with versatility. Our study may suggest a reference for exploring MXenes’ oxidation chemistry and catalytic function and a full understanding of their chemical and biological activities.

Author contributions

He WW developed the concept and conceived the experiments. Jia HM and Liu Quan carried out the main experiments and wrote the manuscript. Chen YY and Zhou G performed partial experiments. Si JJ, Lan HH and He WW revised the manuscript. All the authors contributed to the data analysis and scientific discussion.

Conflicts of interest

The authors declare no conflict of interest.

Acknowledgements

This work is supported financially by National Natural Science Foundation of China (Grants 62274141, 22301258) and the National College Students’ innovation and entrepreneurship training program (202210480001).

References

- 1 Á. Morales-García, F. Calle-Vallejo and F. Illas, *ACS Catal.*, 2020, **10**, 13487–13503.
- 2 L. Chen, X. Y. Dai, W. Feng and Y. Chen, *Acc. Chem. Res.*, 2022, **3**, 785–798.
- 3 Z. M. Qiu, Y. Bai, Y. D. Gao, C. L. Liu, Y. Ru, Y. C. Pi, Y. Z. Zhang, Y. S. Luo and H. Pang, *Rare Met.*, 2022, **41**, 1101–1128.
- 4 Y. Cheng, L. Li, Z. Liu, S. Yan, F. Cheng, Y. Yue, S. Jia, J. Wang, Y. Gao and L. Li, *Research*, 2022, **2022**, 9843268.
- 5 Y. Cheng, Y. Xie, H. Cao, L. Li, Z. Liu, S. Yan, Y. Ma, W. Liu, Y. Yue, J. Wang, Y. Gao and L. Li, *Chem. Eng. J.*, 2023, **453**, 139823.
- 6 M. Naguib, V. N. Mochalin, M. W. Barsoum and Y. J. A. m. Gogotsi, *Adv. Mater.*, 2014, **26**, 992–1005.
- 7 R. M. S. Yoo and A. Djire, *ACS Catal.*, 2023, **13**, 6823–6836.
- 8 X. S. Lv, L. Z. Kou and T. Frauenheim, *ACS Appl. Mater. Interfaces*, 2021, **13**, 14283–14290.
- 9 X. S. Sun, X. J. He, Y. Zhu, E. Obeng, B. R. Zeng, H. Deng, J. I. Shen and R. D. Hu, *Chem. Eng. J.*, 2023, **451**, 138985.
- 10 Z. L. Tan, J. X. Wei, Y. Liu, F. u. Zaman, W. Rehman, L. R. Hou and C. Z. Yuan, *Rare Met.*, 2022, **41**, 775–797.
- 11 Y. Cheng, Y. Xie, Z. Liu, S. Yan, Y. Ma, Y. Yue, J. Wang, Y. Gao and L. Li, *ACS Nano*, 2023, **17**, 1393–1402.
- 12 Y. Cheng, Y. Xie, Y. Ma, M. Wang, Y. Zhang, Z. Liu, S. Yan, N. Ma, M. Liu, Y. Yue, J. Wang and L. Li, *Nano Energy*, 2023, **107**, 108131.
- 13 H. Huang, C. h. Dong, W. Feng, Y. Wang, B. c. Huang and Y. Chen, *Adv. Drug Delivery Rev.*, 2022, **184**, 114178.



14 J. L. Wu, Y. Y. Yu and G. X. Su, *Nanomaterials*, 2022, **12**, 828.

15 Y. Cheng, Y. Xie, S. Yan, Z. Liu, Y. Ma, Y. Yue, J. Wang, Y. Gao and L. Li, *Sci. Bull.*, 2022, **67**, 2216–2224.

16 L. Li, Y. Cheng, H. Cao, Z. Liang, Z. Liu, S. Yan, L. Li, S. Jia, J. Wang and Y. Gao, *Nano Energy*, 2022, **95**, 106986.

17 R. A. Soomro, P. Zhang, B. M. Fan, Y. Wei and B. Xu, *Nano Micro Lett.*, 2023, **15**, 108.

18 F. C. Cao, Y. Zhang, H. Q. Wang, K. Khan, A. K. Tareen, W. Qian, H. Zhang and H. Ågren, *Adv. Mater.*, 2022, **34**, 2107554.

19 X. F. Zhao, A. Vashisth, E. Prehn, W. M. Sun, S. A. Shah, T. Habib, Y. Chen, Z. Tan, J. L. Lutkenhaus and M. Radovic, *Green Matter.*, 2019, **1**, 513–526.

20 H. Q. Geng, Y. P. Ren, G. Qin, T. Wen, Q. Liu, H. Y. Xu and W. W. He, *RSC Adv.*, 2022, **12**, 11128–11138.

21 Y. Li, R. Z. Fu, Z. G. Duan, C. H. Zhu and D. D. Fan, *ACS Nano*, 2022, **16**, 7486–7502.

22 W. Feng, X. G. Han, H. Hu, M. Q. Chang, L. Ding, H. J. Xiang, Y. Chen and Y. H. Li, *Nat. Commun.*, 2021, **12**, 2203.

23 X. Zhao, L. Y. Wang, J. M. Li, L. M. Peng, C. Y. Tang, X. J. Zha, K. Ke, M. B. Yang, B. H. Su and W. Yang, *Adv. Sci.*, 2021, **8**, 2101498.

24 C. J. Du, W. Feng, X. Y. Dai, J. H. Wang, D. Y. Geng, X. D. Li, Y. Chen and J. Zhang, *Small*, 2022, **18**, 2203031.

25 X. Y. Ren, M. F. Huo, M. M. Wang, H. Lin, X. X. Zhang, J. Yin, Y. Chen and H. H. Chen, *ACS Nano*, 2019, **13**, 6438–6454.

26 R. F. Zhang, X. Y. Yan and K. L. Fan, *Acc. Chem. Res.*, 2021, **2**, 534–547.

27 H. Wei, L. Z. Gao, K. L. Fan, J. W. Liu, J. Y. He, X. G. Qu, S. J. Dong, E. K. Wang and X. Y. Yan, *Nano Today*, 2021, **40**, 101269.

28 Q. Yang, Y. Y. Mao, Q. Liu and W. W. He, *Rare Met.*, 2023, **42**, 2928–2948.

29 Y. Wei, P. Zhang, R. A. Soomro, Q. Z. Zhu and B. Xu, *Adv. Mater.*, 2021, **33**, 2103148.

30 X. Wang, S. Lin, H. Y. Tong, Y. N. Huang, P. Tong, B. C. Zhao, J. M. Dai, C. H. Liang, H. Wang, X. B. Zhu, Y. P. Sun and S. X. Dou, *Electrochim. Acta*, 2019, **307**, 414–421.

31 Y. Liu, Y. Jiang, Z. Hu, J. Peng, W. H. Lai, D. L. Wu, S. W. Zuo, J. Zhang, B. Chen, Z. W. Dai, Y. G. Yang, Y. Huang, W. Zhang, W. Zhao, W. Zhang, L. Wang and S. L. Chou, *Adv. Funct. Mater.*, 2020, **31**, 2008033.

32 L. Z. Gao, J. Zhuang, L. Nie, J. B. Zhang, Y. Zhang, N. Gu, T. H. Wang, J. Feng, D. L. Yang, S. Perrett and X. Yan, *Nat. Nanotechnol.*, 2007, **2**, 577–583.

33 H. J. Dong, W. Du, J. Dong, R. C. Che, F. Kong, W. L. Cheng, M. Ma, N. Gu and Y. Zhang, *Nat. Commun.*, 2022, **13**, 5365.

34 R. R. Langeslay, D. M. Kaphan, C. L. Marshall, P. C. Stair, A. P. Sattelberger and M. Delferro, *Chem. Rev.*, 2019, **119**, 2128–2191.

35 F. A. Cotton, G. Wilkinson, C. A. Murillo and M. Bochmann, *Adv. Inorg. Chem.*, John Wiley and Sons, Inc., 1999.

36 G. D. Du and J. H. Espenson, *Inorg. Chem.*, 2005, **44**, 5514–5522.

